

Turbo Coded Single Sideband OFDM-OQAM Signaling through Frequency Selective Rayleigh Fading Channels

Kasturi Vasudevan ¹ 

¹ IIT Kanpur; vasu@iitk.ac.in

Abstract

This work investigates the bit-error-rate (BER) performance of turbo coded orthogonal frequency division multiplexed - offset quadrature amplitude modulated (OFDM- OQAM) signals transmitted through frequency selective Rayleigh fading channels in the presence of carrier frequency offset (CFO) and additive white Gaussian noise (AWGN). The highlight of this work is to use the root raised cosine (RRC) pulse and its Hilbert transform as the complex-valued transmit filter and a simple matched filter at the receiver. The proposed system is similar to single sideband (SSB) modulation, that has roots in analog communications. Turbo code and subcarrier diversity is employed to improve the BER performance over that of an uncoded system. Discrete-time algorithms for frame detection, two-step CFO, channel and noise variance estimation have been proposed. A single transmit and receive antenna is assumed. Similar work has not been done earlier.

Keywords: OFDM-OQAM; Hilbert transform; single sideband modulation; turbo code; frequency selective Rayleigh fading channel; carrier frequency offset; synchronization; subcarrier diversity.

1. Introduction

Orthogonal frequency division multiplexing-offset quadrature amplitude modulation (OFDM-OQAM) is a modulation of choice for 5G and beyond technologies due to its spectral containment and robustness to carrier frequency offset (CFO), compared to classical OFDM. However, it has been shown in [1–3] that CFO in OFDM can be estimated very accurately with linear complexity and large scope for parallel processing. Moreover, the spectrum of OFDM can also be contained using pulse shaping [4]. The overhead due to the cyclic prefix (CP) in OFDM can be reduced by increasing the “frame” size. In fact it is the “training” or “pilot” that increases the overhead, rather than CP [1–3]. Most of the literature on OFDM-OQAM or its variants like filter bank multicarrier (FBMC) or universal filtered multicarrier (UFMC), use non-Nyquist pulses like isotropic orthogonal transfer algorithm (IOTA) and extended Gaussian functions (EGF), which result in intersymbol interference (ISI) [5–10]. A brief survey of OFDM-OQAM is given below.

Channel estimation for coherent optical FBMC-OQAM is given in [11]. Underwater acoustic communications using FBMC-OQAM is presented in [12]. FBMC for massive multiple input multiple output (MIMO) systems is investigated in [13,14]. Blind joint CFO and sampling time offset (STO) estimation for FBMC-OQAM systems is addressed in [15]. Downlink precoding for cell-free FBMC/OQAM systems with asynchronous reception is considered in [16]. FBMC-OQAM transceivers for 6G and beyond has been reviewed in [17]. A low-complexity symbol reconstruction based on direct symbol decision for FBMC-OQAM systems is presented in [18]. The performance of FBMC and OFDM in fiber optic

Received:
Revised:
Accepted:
Published:

Citation: Vasudevan, K. Title. *Journal Not Specified* **2025**, *1*, 0.
<https://doi.org/>

Copyright: © 2026 by the author. Submitted to *Journal Not Specified* for possible open access publication under the terms and conditions of the Creative Commons Attribution (CC BY) license (<https://creativecommons.org/licenses/by/4.0/>).

arXiv:2602.18881v1 [cs.IT] 21 Feb 2026

systems is studied in [19]. A nonuniform FBMC-OQAM with subchannels having arbitrary bandwidths is discussed in [20]. Voice transmission over voiceband channels using FBMC-OQAM is presented in [21]. Design of waveforms for FBMC-OQAM is considered in [22,23]. Peak-to-average power ratio (PAPR) reduction in FBMC-OQAM is given in [24]. Detection of OFDM-OQAM signals in the presence of phase noise is discussed in [25]. A new pilot pattern for channel estimation in FBMC systems is considered in [26].

In [27], an efficient channel estimation for UFMC is proposed. In [28], it is shown that the BER performance of full duplex (FD) FBMC (FD-FBMC) is better than FD-UFMC and FD-OFDM. A reliability-based signal detection for UFMC is proposed in [29]. Sparse code multiple access in UFMC is presented in [30]. A performance comparison between OFDM and UFMC for passive optical networks (PON) is studied in [31]. A deep learning-aided signal detection for two-stage index modulated UFMC systems is proposed in [32]. Multiple access techniques for OFDM, FBMC and UFMC is presented in [33]. Blind carrier frequency offset (CFO) estimation in UFMC is investigated in [34,35]. Performance comparison of FBMC, UFMC and filtered OFDM (F-OFDM) is given in [36]. UFMC for MIMO systems is addressed in [37]. Peak-to-average power ratio (PAPR) reduction in OFDM, F-OFDM and UFMC is discussed in [38]. UFMC over optical fiber networks for 6G is investigated in [39]. A low complexity UFMC receiver for 6G is given in [40].

In this work, we use the pulse having the root raised cosine (RRC) spectrum and its modified Hilbert transform as the complex-valued transmit filter. This approach also corresponds to single sideband (SSB) modulation that has roots in analog communications. Therefore, the bandwidth of the transmitted signal is half that of conventional QAM or OQAM systems and is narrow enough such that the channel can be considered to be distortionless, justifying the use of a matched filter receiver [4,41,42]. In practice however, the distortionless channel assumption may not strictly hold, which results in ISI. The bit-error-rate (BER) performance of the proposed system has been analyzed using computer simulations in the presence of carrier frequency offset (CFO), frequency selective Rayleigh fading channel and additive white Gaussian noise (AWGN). Turbo coding and subcarrier diversity has been introduced to significantly improve the BER performance over that of the uncoded system. Discrete-time algorithms for frame detection, CFO, channel and noise variance estimation have been discussed. Similar work has not been done earlier.

This paper is organized as follows. Section 2 presents the system model. In section 3, we describe the discrete-time receiver algorithms. Section 4 contains the simulation results. Finally, the conclusions are in section 5.

The notation used is as follows. Complex quantities are denoted by tilde, e.g. \tilde{x} . Caret is used to denote estimate [4] or Hilbert transform [43], depending on the context, e.g. \hat{x} denotes estimate or Hilbert transform of x . However, we emphasize that by default, caret denotes an estimate. If it denotes Hilbert transform, then it is explicitly stated. Boldface is used for vectors and matrices. The letter “ j ” denotes $\sqrt{-1}$, “ \star ” denotes convolution and “ $E[\cdot]$ ” is the expectation operator. “ $\Re\{\cdot\}$ ” denotes the real part and “ $\Im\{\cdot\}$ ” denotes imaginary part of a complex quantity.

2. System Model

The block diagram of the proposed discrete-time OFDM-OQAM system is shown in Figure 1. Here subcarrier diversity is used, that is, the same information is transmitted over multiple subcarriers to improve the BER performance. A single transmit and receive

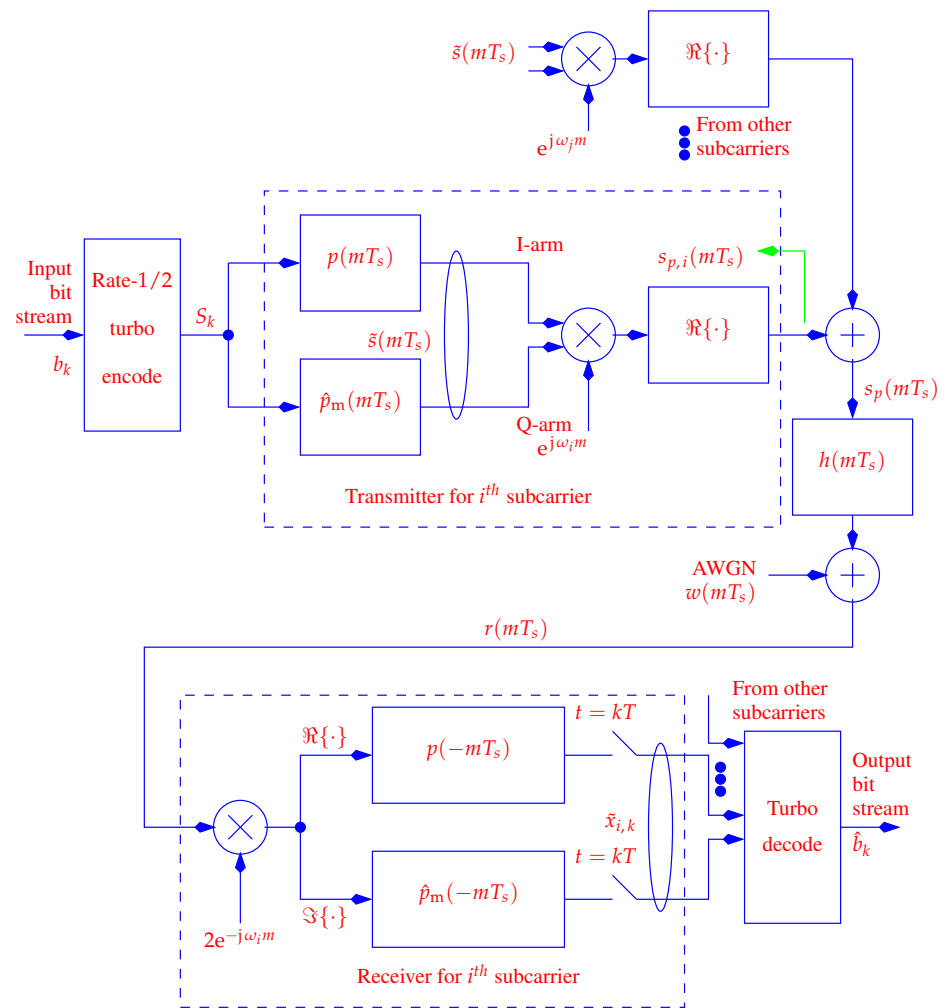


Figure 1. Discrete-time system model of OFDM-OQAM.

antenna (single input single output (SISO)) is assumed. The complex baseband signal at the transmitter is given by [41]

$$\tilde{s}(mT_s) = \sum_{k=0}^{L_d-1} S_k \tilde{p}_m(mT_s - kT) \quad (1)$$

where L_d is the frame length in bits, $1/T$ is the symbol rate, $1/T_s$ is the sampling frequency and $\tilde{p}_m(\cdot)$ is the complex-valued transmit filter given by [41]

$$\tilde{p}_m(mT_s) = p(mT_s) + j \hat{p}_m(mT_s) \quad (2)$$

where $p(\cdot)$ is the pulse having the root-raised cosine (RRC) spectrum and $\hat{p}_m(\cdot)$ is the pulse corresponding to the modified Hilbert transform of the RRC (mHT-RRC) spectrum [41]. We assume that the interpolation factor is [41]

$$\frac{T}{T_s} = I \quad (\text{an integer}). \quad (3)$$

The spectrum of the signal in (1) extends over [4]

$$\begin{aligned} 0 \leq \omega \leq \frac{\pi(1+\rho)}{I} \\ \Rightarrow \text{bandwidth} = \frac{\pi(1+\rho)}{I} \end{aligned} \quad (4)$$

where ω is the digital frequency in radians and $0 < \rho \leq 1$ is the roll-off factor of the RRC spectrum. Thus (1) is a single sideband (SSB) signal. Since a rate-1/2 turbo code is used, the frame contains both data and parity bits, which are mapped to BPSK with amplitude $S_k \in \pm 1$. We assume that bit 0 maps to +1 and bit 1 maps to -1. The frame also contains training bits, which are distributed at random time slots over the frame and spans the entire frame. Therefore, the first and last bits of the frame correspond to training. This is illustrated in Figure 2. The number of data bits in a frame is

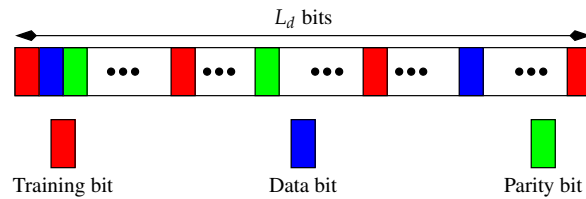


Figure 2. Proposed frame structure of OFDM-OQAM.

$$L_{d1} = L_d/3 \quad (5)$$

since the frame contains equal number of data, parity and training bits. The generating matrix of the constituent encoder of the turbo code is given by [1-4,41,44-49]

$$\mathbf{G}(D) = \begin{bmatrix} 1 & \frac{1+D^2}{1+D+D^2} \end{bmatrix}. \quad (6)$$

The passband signal for the i^{th} subcarrier is given by

$$s_{p,i}(mT_s) = \Re \left\{ \tilde{s}(mT_s) e^{j\omega_i m} \right\} \quad (7)$$

where ω_i is the digital carrier frequency given by

$$\omega_i = \frac{2\pi k_i}{I} + \delta_i \quad (8)$$

where $1 \leq k_i < I/2$ is an integer and δ_i is the frequency offset in the i^{th} subcarrier, in radians. Note that $k_i = 0$ corresponds to the baseband signal (no modulation), and is hence not used. In this work, we assume that the frequency offset is at most $\pm 1\%$ of the symbol rate ($1/T$). This implies that

$$\delta_i \in \left[-\frac{\pi}{50I}, \frac{\pi}{50I} \right] \quad (9)$$

where I is given in (3). Let

$$\delta_{\max} = \frac{\pi}{50I}. \quad (10)$$

We assume that the frequency offset δ_i is uniformly distributed in $[-\delta_{\max}, \delta_{\max}]$. The overall discrete-time transmitted passband signal is given by

$$s_p(mT_s) = \sum_{i=1}^{N_{\text{sc}}} s_{p,i}(mT_s) \quad (11)$$

where N_{sc} denotes the number of subcarriers (subcarrier diversity). The discrete-time signal at the receiver input is

$$\begin{aligned} r(mT_s) &= s_p(mT_s) \star h(mT_s) + w(mT_s) \\ &= \sum_{l=0}^{L_h-1} h(lT_s) s_p(mT_s - lT_s) + w(mT_s) \end{aligned} \quad (12)$$

where $h(\cdot)$ denotes the impulse response of the real-valued, quasi-static, frequency selective fading channel, L_h denotes the channel length and $w(mT_s)$ denotes samples of real-valued AWGN with zero-mean and variance σ_w^2 . The ‘‘quasi-static’’ assumption implies that the channel impulse response is time-invariant over one frame and varies independently from frame-to-frame. The channel coefficients are real-valued, wide sense stationary (WSS), independent, zero-mean Gaussian random variables with variance $1/L_h$, that is

$$\begin{aligned} E[h(lT_s)h(lT_s - mT_s)] &= \frac{\delta_K(mT_s)}{L_h} \\ &\triangleq R_{hh}(mT_s) \end{aligned} \quad (13)$$

where $\delta_K(\cdot)$ is the Kronecker-delta function [4,50]. Assuming a flat fading channel for each subcarrier, which is true if the signal bandwidth around the subcarrier is sufficiently narrow (I in (4) is sufficiently large) [4,41], the signal at the matched filter output for the i^{th} subcarrier at the k^{th} symbol instant can be written as

$$\tilde{x}_{i,k} = \tilde{H}_i S_k (1 + j) + \tilde{z}_{i,k} \quad (14)$$

where $\tilde{z}_{i,k}$ denotes samples of complex-valued AWGN and

$$\begin{aligned}\tilde{H}(\omega) &= \sum_{l=0}^{L_h-1} h(lT_s) e^{-j\omega l} \\ \Rightarrow \tilde{H}_i &\triangleq \tilde{H}(\omega_i)\end{aligned}\quad (15)$$

is the discrete-time Fourier transform (DTFT) of the channel [4,50] and ω_i is given by (8). Since δ_i in (9) is small, ω_i in (8) can be approximated as

$$\omega_i \approx \frac{2\pi k_i}{I}. \quad (16)$$

Using (13) and (16) we get

$$\begin{aligned}E[\tilde{H}_i \tilde{H}_j^*] &= \frac{1}{L_h} \sum_{m=0}^{L_h-1} e^{-j2\pi m(k_i - k_j)/I} \\ &= \delta_K(k_i - k_j)\end{aligned}\quad (17)$$

provided

$$k_i - k_j = \frac{In}{L_h} \quad (18)$$

where n is an integer. Thus (18) specifies the subcarrier spacing required for uncorrelated fading, which is necessary for achieving the minimum BER. Assuming that the filters $p(mT_s)$ and $\hat{p}_m(mT_s)$ have unit energy, the one-dimensional variance of $\tilde{z}_{i,k}$ in (14) is equal to [4]

$$\frac{1}{2} E[|\tilde{z}_{i,k}|^2] = 2\sigma_w^2. \quad (19)$$

Since the information contained in (14) is $1/(2N_{sc})$ bits, the average SNR per bit is given by [45]

$$\begin{aligned}\text{SNR}_{\text{av},b} &= \frac{2 \times 2N_{sc} \times E[|\tilde{H}_i|^2] E[S_k^2]}{E[|\tilde{z}_{i,k}|^2]} \\ &= \frac{N_{sc}}{\sigma_w^2}\end{aligned}\quad (20)$$

where we have used (17) and (19). In the next section, we discuss the receiver algorithms.

3. Receiver Algorithms

3.1. Frequency Offset and Frame Detection

The first step is to detect the presence of a frame. Assuming a worst case frequency offset of $\delta_{\max} = \pi/(50I)$ and a typical frame size of $L_d = 3L_{d1} = 1536$ bits or $L_d I$ samples, the phase change due the frequency offset over the entire frame is

$$\begin{aligned}\Delta\theta &= \frac{\pi}{50I} \times L_d I \\ &= 96.51 \text{ radians}\end{aligned}\quad (21)$$

which is significant. Therefore it is necessary to estimate and cancel the frequency offset. In what follows, we describe the optimum (maximum likelihood (ML)) joint frequency offset and frame detection procedure. Let

$$S_{k,t} = \begin{cases} S_k & \text{if } S_k \text{ is training bit} \\ 0 & \text{otherwise.} \end{cases} \quad (22)$$

In other words, $S_{k,t}$ contains only training bits, with data and parity bits set to zero. Define

$$\begin{aligned} s_{t,I}(mT_s) &= \sum_{k=0}^{L_d-1} S_{k,t} p(mT_s - kT) \\ s_{t,Q}(mT_s) &= \sum_{k=0}^{L_d-1} S_{k,t} \hat{p}_m(mT_s - kT). \end{aligned} \quad (23)$$

Note that $s_{t,I}(mT_s)$ and $s_{t,Q}(mT_s)$ can be precomputed and stored at the receiver. The joint detection is given by

$$\begin{aligned} \max_{\hat{\omega}_i, m} Z(\hat{\omega}_i, m) &= |(2r(mT_s) \cos(\hat{\omega}_i m)) \star s_{t,I}(-mT_s) \\ &\quad - j (2r(mT_s) \sin(\hat{\omega}_i m)) \star s_{t,Q}(-mT_s)| \end{aligned} \quad (24)$$

where

$$\hat{\omega}_i = \frac{2\pi k_i}{I} + \hat{\delta}_i. \quad (25)$$

Note that (24) corresponds to demodulation followed by matched filtering by the baseband training signals given in (23). The signals $s_{t,I}(-mT_s)$ and $s_{t,Q}(-mT_s)$ in (24) are referred to as “baseband training matched filters”. The frequency offset is estimated using

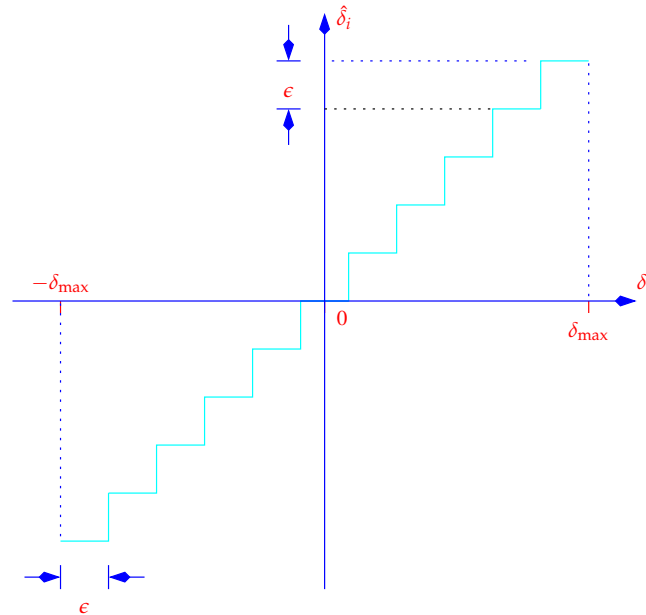


Figure 3. Mid-step quantizer for frequency offset estimation.

a uniform mid-step quantizer (a uniform mid-rise quantizer can also be used) [43,51]. The

interval $[-\delta_{\max}, \delta_{\max}]$ is divided into B intervals, where B is an odd integer, as shown in Figure 3, for $B = 11$. The step-size is

$$\epsilon = \frac{2\delta_{\max}}{B} \text{ radians.} \quad (26)$$

Clearly from Figure 3, the maximum error in the frequency offset estimate is $\pm\epsilon/2$. We restrict the phase change due to error in the frequency offset estimate (residual frequency offset) over the whole frame to 0.1π . Hence we obtain

$$\begin{aligned} \frac{\epsilon}{2}L_dI &= 0.1\pi \text{ radians} \\ \Rightarrow \frac{\delta_{\max}}{B}L_dI &= 0.1\pi \\ \Rightarrow \frac{\pi}{50IB}L_dI &= 0.1\pi \\ \Rightarrow B &= \frac{L_d}{5}. \end{aligned} \quad (27)$$

For a typical value of $L_d = 1536$ bits, we get $B = 307.2 \equiv 309$ (next higher odd integer) intervals. Thus with $I = 16$, the complexity of (24) is of the order of $\mathcal{O}(L_dIB) = 7,593,984$ operations (additions, subtractions and multiplications) for each subcarrier, which is quite large. Therefore, we next describe the two-step approach for frequency offset estimation, which is much more efficient. In the first step, namely coarse, we constrain the phase change due to residual frequency offset over the entire frame to

$$\begin{aligned} \frac{\epsilon_c}{2}L_dI &= \pi \text{ radians} \\ \Rightarrow \frac{\delta_{\max}}{B_c}L_dI &= \pi \\ \Rightarrow \frac{\pi}{50IB_c}L_dI &= \pi \\ \Rightarrow B_c &= \frac{L_d}{50} \end{aligned} \quad (28)$$

where

$$\epsilon_c = \frac{2\delta_{\max}}{B_c} \text{ radians.} \quad (29)$$

Using $L_d = 1536$, we get $B_c = 30.72 \equiv 31$ (odd integer). Clearly, the savings in computation in (28) over (27) is by a factor of

$$\frac{B}{B_c} = 10. \quad (30)$$

The result of coarse frequency offset estimate obtained from (24), using B_c intervals, is shown in Figure 4, at an average SNR per bit of zero dB, and random frequency offset in the range given in (9). The interpolation factor is $I = 16$, the index of the second subcarrier is $k_2 = 3$ and the roll-off factor of the RRC spectrum is $\rho = 0.161$. Hence, the subcarrier frequency is $2\pi k_2/I = 1.1781$ radians and from (4) we obtain the signal bandwidth as 0.228 radians on one (upper) side the subcarrier frequency. The channel magnitude response used to obtain Figure 4, is shown in Figure 5, with $\omega = 2\pi l/512$, for $0 \leq l < 512$ and channel length $L_h = 8$ coefficients (see also (15)). The signal bandwidth is also shown in Figure 5. Note that for coarse frequency offset estimation, ϵ in Figure 3 must be replaced by ϵ_c and $\hat{\delta}_i$ must be replaced by $\hat{\delta}_{i,c}$. Consequently, $\hat{\omega}_i$ in (24) must be replaced by $\hat{\omega}_{i,c}$, where

$$\hat{\omega}_{i,c} = \frac{2\pi k_i}{I} + \hat{\delta}_{i,c}. \quad (31)$$

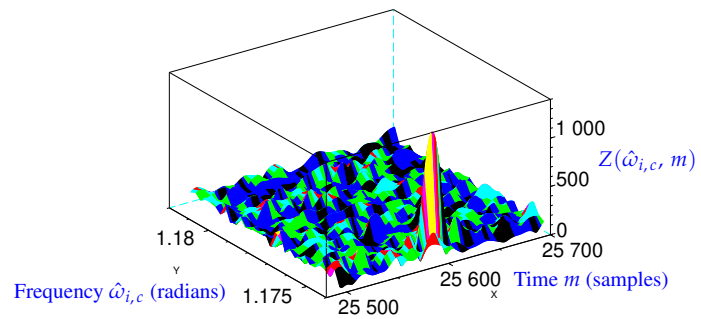


Figure 4. Coarse frequency offset and frame detection.

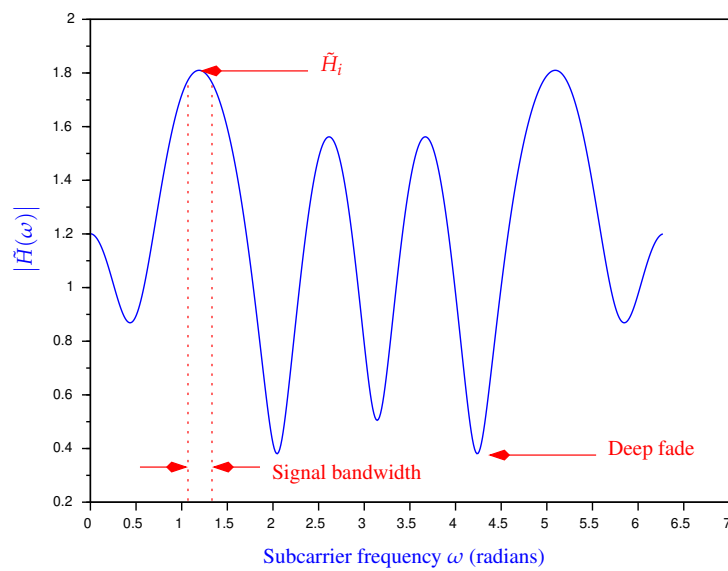


Figure 5. Channel magnitude response from 0 to 2π radians.

Let $\hat{\delta}_{i,c}$ denote the coarse estimate of the frequency offset obtained from (24), using B_c intervals of size ϵ_c . Next, fine frequency offset estimate needs to be obtained. This is done by considering the residual frequency offset to be in the range $[\hat{\delta}_{i,c} - \epsilon_c, \hat{\delta}_{i,c} + \epsilon_c]$ and dividing this range into $B_f = 21$ intervals. If the actual frequency offset δ_i lies outside this range, it is said to be an *outlier*. The size of each interval during fine frequency offset estimation is

$$\begin{aligned}\epsilon_f &= \frac{2\epsilon_c}{B_f} \\ &= \frac{2 \times 2\delta_{\max}}{B_c B_f} \text{ radians.}\end{aligned}\quad (32)$$

Assuming an error in the fine frequency offset estimate to be $\pm\epsilon_f/2$, the phase change due to the residual frequency offset estimate over the entire frame is

$$\begin{aligned}\frac{\epsilon_f}{2} L_d I &= \frac{2\delta_{\max}}{B_c B_f} L_d I \\ &= \frac{2\pi}{50 B_c B_f} L_d I \\ &= 0.09\pi \\ &< 0.1\pi\end{aligned}\quad (33)$$

for $L_d = 1536$, $B_c = 31$ and $B_f = 21$. The result of fine frequency offset estimation and

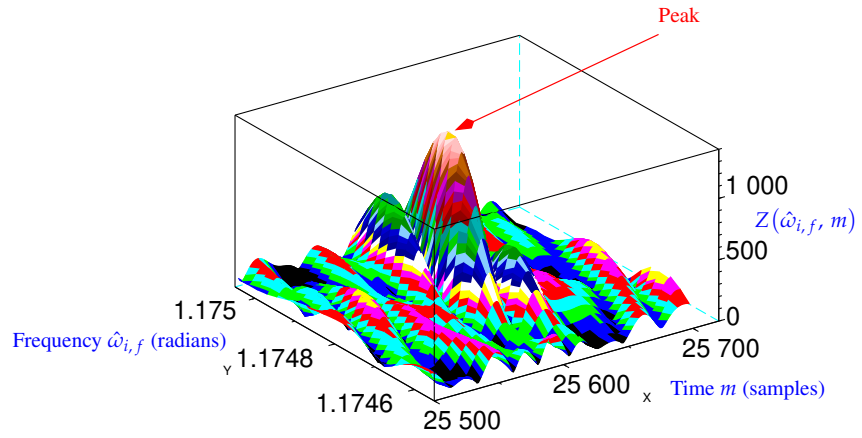


Figure 6. Fine frequency offset and frame detection.

frame detection using (24) is shown in Figure 6, at an average SNR per bit equal to zero dB. Observe that for fine frequency offset estimation, δ_{\max} in Figure 3 must be replaced by $\hat{\delta}_{i,c} + \epsilon_c$, $-\delta_{\max}$ must be replaced by $\hat{\delta}_{i,c} - \epsilon_c$, ϵ must be replaced by ϵ_f as given in (32) and δ_i must be replaced by $\hat{\delta}_{i,f}$. Similarly, $\hat{\omega}_i$ in (24) must be replaced by $\hat{\omega}_{i,f}$ where

$$\hat{\omega}_{i,f} = \hat{\omega}_{i,c} + \hat{\delta}_{i,f} \quad (34)$$

where $\hat{\omega}_{i,c}$ is given in (31).

We conclude this subsection with the following observations:

1. The joint frequency offset and frame detection procedure in (24) has a lot of scope for parallel processing.

2. Observe that $\hat{\omega}_i$ in (24) must be replaced by $\hat{\omega}_{i,c}$ for coarse frequency offset estimation and by $\hat{\omega}_{i,f}$ for fine frequency offset estimation.
3. The frame is “detected” during fine frequency offset estimation by computing the peak-to-average (PTA) value of $Z^2(\hat{\omega}_{i,f}, m)$ over all $\hat{\omega}_{i,f}$ and m in (24). The frame is declared as “detected” if $\text{PTA} > 100$ for at least one subcarrier. Conversely, the frame transmitted over a subcarrier in deep fade, as illustrated in Figure 5, may not be detected, if $\text{PTA} < 100$. If all the subcarriers are simultaneously in deep fade, then the frame may not be detected. This is referred to as an “erasure” [52].
4. The computational complexity per subcarrier for the two-stage approach is

$$\mathcal{O}(L_d I(B_c + B_f)) \quad (35)$$

whereas for the single-stage approach it is $\mathcal{O}(L_d I B)$. Hence, the savings in computation is by a factor of

$$\frac{B}{B_c + B_f} = 5.9 \quad (36)$$

for $B = 309$, $B_c = 31$ and $B_f = 21$.

5. Once the frame is “detected”, it is straightforward to compute the sampling instants $t = kT$ at the output of the two matched filters (see Figure 1), in order to obtain (14), and accounting for the training bits. Since the “peak” (see Figure 6) is obtained at the end of the frame (recall that the first and last bits of the frame correspond to training, as shown in Figure 2), it coincides with the last training bit. Therefore, the remaining bits in the frame can be obtained by starting from the “peak”, going backwards in time, and downsampling the matched filter outputs by a factor of I .
6. The root mean squared (RMS) coarse frequency offset estimation error is given by

$$\omega_{e,\text{rms},c} = \left(\overline{(\omega_i - \hat{\omega}_{i,c})^2} \right)^{1/2} \quad (37)$$

where $\overline{(\cdot)}$ denotes time average over all frames and subcarriers, ω_i is given in (8) and $\hat{\omega}_{i,c}$ is given in (31). Similarly, the RMS fine frequency offset estimation error is

$$\omega_{e,\text{rms},f} = \left(\overline{(\omega_i - \hat{\omega}_{i,f})^2} \right)^{1/2} \quad (38)$$

where, the time average is taken over all *detected* frames and subcarriers and $\hat{\omega}_{i,f}$ is given in (34).

In the next subsection, we discuss channel and noise variance estimation.

3.2. Channel and Noise Variance Estimation

From Figure 5, it is clear that the signal bandwidth is narrow enough for the channel to be considered ideal (channel magnitude response is flat and phase response is linear). Therefore, it is only necessary to estimate \tilde{H}_i in (14) and (15). Observe that the term inside the magnitude in (24) corresponding to the peak (see Figure 6) during fine frequency offset estimation is equal to (see also (14))

$$\tilde{Z}_{\max}(\hat{\omega}_{i,f}, m) = L_{d1} \tilde{H}_i (1 + j) + \tilde{z}_{1,i,m} \quad (39)$$

where it is assumed that there are L_{d1} training bits, the filters $p(mT_s)$ and $\hat{p}_m(mT_s)$ have unit energy and $\tilde{z}_{1,i,m}$ denotes complex valued noise. It can be shown that the variance per dimension of $\tilde{z}_{1,i,m}$ is (see also (19))

$$\frac{1}{2}E\left[|\tilde{z}_{1,i,m}|^2\right] = 2L_{d1}\sigma_w^2. \quad (40)$$

Observe that since (39) is the peak output of the training matched filter, the SNR is maximized [4]. The statement of the maximum likelihood (ML) channel estimation problem is as follows [1–3,46]: find \hat{H}_i such that

$$\left|\tilde{Z}_{\max}(\hat{\omega}_{i,f}, m) - L_{d1}\hat{H}_i(1+j)\right|^2 \quad (41)$$

is minimized. Differentiating (41) with respect to \hat{H}_i^* [4] and setting the result to zero, we obtain

$$\hat{H}_i = \frac{\tilde{Z}_{\max}(\hat{\omega}_{i,f}, m)}{(1+j)L_{d1}}. \quad (42)$$

The RMS channel estimation error is given by

$$H_{e,\text{rms}} = \left(\overline{\left(|\tilde{H}_i| - |\hat{H}_i|\right)^2}\right)^{1/2} \quad (43)$$

where the time average is taken over all detected frames and subcarriers, \hat{H}_i is given in (42) and \tilde{H}_i is given in (15). Observe that the difference of the absolute values is taken in (43), since \hat{H}_i may contain an unknown carrier phase.

The next step is to estimate the two-dimensional noise variance at the matched filter output, since it is required for turbo decoding [4]. Let k_t denote the time instant corresponding training bit. Then the estimate of the one-dimensional noise variance for the i^{th} subcarrier is given by

$$\hat{\sigma}_{w,i}^2 = \frac{1}{2L_{d1}} \sum_{\substack{k=0 \\ k \in k_t}}^{L_d-1} \left| \tilde{x}_{i,k} - \hat{H}_i(1+j)S_{k,t} \right|^2 \quad (44)$$

where \hat{H}_i is given in (42) and $S_{k,t}$ is given in (22). Note that the estimate of the one-dimensional noise variance at the output of the matched filters is $2\hat{\sigma}_{w,i}^2$ (see also (19)). The RMS error in the estimation of the two-dimensional noise variance at the matched filter outputs is

$$\sigma_{e,\text{rms,MFop}}^2 = \left(\overline{\left(4\sigma_w^2 - 4\hat{\sigma}_{w,i}^2\right)^2}\right)^{1/2} \quad (45)$$

where the time average is taken over all detected frames and subcarriers. In the next subsection, we briefly discuss turbo decoding using the BCJR algorithm [4,53].

3.3. Turbo Decoding

Turbo decoding using the BCJR algorithm has been discussed extensively in [4], and hence will not be repeated here, except for specific details. We begin by observing that the data and parity bits are distributed across random time slots in the frame, since the training bits are also at random time slots, other than the first and last slot. Hence, for the purpose of turbo decoding, the data and parity bits have to be re-arranged to consecutive time slots, denoted by k_r , for $0 \leq k_r \leq L_{d1} - 1$. We assume that this has been done. Let $\tilde{x}_{i,k_r,b1}$ denote the data sample, $\tilde{x}_{i,k_r,c1}$ denote the parity sample from encoder 1 and $\tilde{x}_{i,k_r,c2}$

the parity sample from encoder 2, all extracted and re-arranged from $\tilde{x}_{i,k}$ in (14). Since a rate-1/2 turbo code is used, $\tilde{x}_{i,k_r,c1}$ is defined only for even values of k_r , whereas $\tilde{x}_{i,k_r,c2}$ is defined only for odd values of k_r . Following the notation in [4], for a trellis transition at time k_r , from encoder state e to f at decoder 1

$$\gamma_{1,\text{sys},k_r,e,f} = \exp\left[-d_{k_r,b1,e,f}^2\right] \quad (46)$$

where

$$d_{k_r,b1,e,f}^2 = \sum_{i=1}^{N_{\text{sc},d}} \frac{|\tilde{x}_{i,k_r,b1} - \hat{H}_i S_{b,e,f}|^2}{2\hat{\sigma}_{w,i}^2} \quad (47)$$

where $N_{\text{sc},d} \leq N_{\text{sc}}$ is the number of detected subcarriers, $S_{b,e,f} \in \pm 1$ is the systematic (data) bit corresponding to the transition from encoder state e to f , \hat{H}_i is given in (42) and $\hat{\sigma}_{w,i}^2$ is given in (44). Similarly

$$\gamma_{1,\text{par},k_r,e,f} = \begin{cases} \exp\left[-d_{k_r,c1,e,f}^2\right] & \text{for even } k_r \\ 1 & \text{otherwise} \end{cases} \quad (48)$$

where

$$d_{k_r,c1,e,f}^2 = \sum_{i=1}^{N_{\text{sc},d}} \frac{|\tilde{x}_{i,k_r,c1} - \hat{H}_i S_{c,e,f}|^2}{2\hat{\sigma}_{w,i}^2} \quad (49)$$

where $S_{c,e,f} \in \pm 1$ is the parity bit corresponding to the transition from encoder state e to f . The equations for decoder 2 are similar, excepting that $\tilde{x}_{i,k_r,b2}$ and $\tilde{x}_{i,k_r,c2}$ have to be used. Note that $\tilde{x}_{i,k_r,b2}$ is the interleaved version of $\tilde{x}_{i,k_r,b1}$. Moreover $\gamma_{2,\text{par},k_r,e,f}$ has to be set to unity for even k_r , unlike $\gamma_{1,\text{par},k_r,e,f}$ in (48). In the next section we discuss computer simulation results.

4. Results

The simulation parameters are shown in Table 1. The BER results for $N_{\text{sc}} = 1$ is

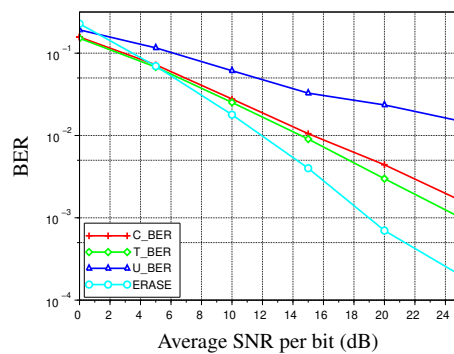
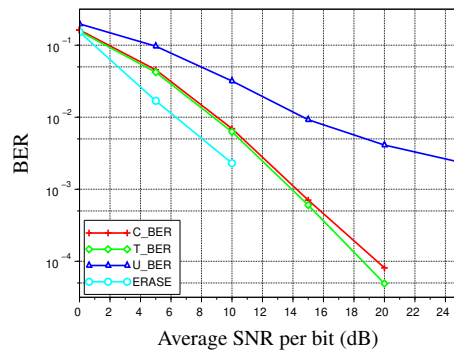
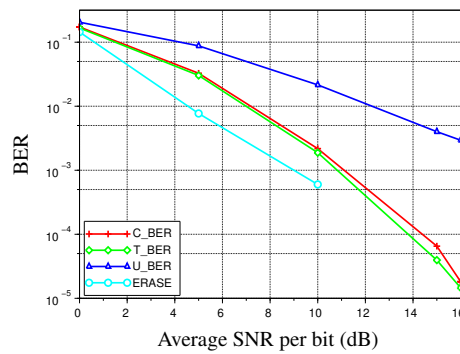


Figure 7. BER results for $N_{\text{sc}} = 1$.

shown in Figure 7. Here “C_BER” denotes the turbo coded BER from simulations, “T_BER” is the theoretical BER from [49], “U_BER” is the simulated uncoded BER and “ERASE” is the probability of erasure [52]. Observe the close match between C_BER and T_BER. The simulation results for $N_{\text{sc}} = 2, 3, 4$ are presented in Figures 8-10. The following observations can be made from Figures 7-10:

Table 1. Simulation parameters.

Parameter	Value
Interpolation factor I	16
Subcarrier diversity N_{sc}	1, 2, 3, 4
Channel length L_h	8
Transmit antenna	1
Receive antenna	1
Frame size L_d in bits	1536
Data size L_{d1} in bits	512
Peak-to-average (PTA) threshold	100
Max carrier frequency offset	$\pm \frac{\pi}{50I}$ rad
Frames simulated	10^4
Transmit filter length (samples)	$64I$

**Figure 8.** BER results for $N_{sc} = 2$.**Figure 9.** BER results for $N_{sc} = 3$.

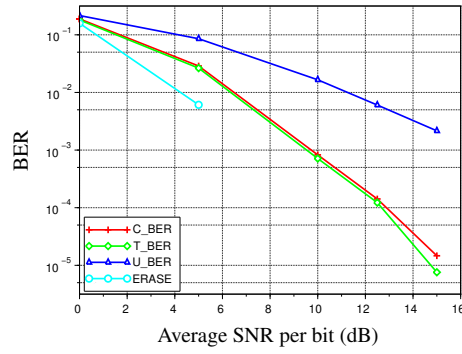


Figure 10. BER results for $N_{sc} = 4$.

1. At a BER of 10^{-4} , there is about 10 dB improvement between $N_{sc} = 1, 2$, about 6 dB improvement between $N_{sc} = 2, 3$ and only about 1 dB improvement between $N_{sc} = 3, 4$. This shows that increasing N_{sc} has diminishing returns.
2. The BER performance may be limited by ISI, since the channel is not distortionless. The BER performance may be improved by increasing the interpolation factor I , for a fixed channel length L_h . This would reduce the signal bandwidth in Figure 5, which would better approximate the distortionless channel assumption. However, increasing I results in increased simulation complexity (see (35)).
3. Increasing the subcarrier diversity N_{sc} results in increased transmission bandwidth, since it is equivalent to frequency division multiplexing. Perhaps antenna diversity is an alternate solution. Therefore, the BER performance of the proposed OFDM-OQAM system can be studied for MIMO systems.
4. The BER performance of turbo coded OFDM-OQAM is far superior to that of uncoded.

Table 2. RMS error at an average SNR per bit of 5 dB. Values in red colour correspond to ideal channel.

Parameter	$N_{sc} = 1$	$N_{sc} = 2$	$N_{sc} = 3$	$N_{sc} = 4$
$\omega_{e,rms,c}$	3.86×10^{-4} 7.3×10^{-5}	5.63×10^{-4} 7.4×10^{-5}	7.47×10^{-4} 7.4×10^{-5}	9.08×10^{-4} 7.4×10^{-5}
$\omega_{e,rms,f}$	3.3×10^{-5} 8×10^{-6}	3.4×10^{-5} 9×10^{-6}	3.3×10^{-5} 9×10^{-6}	3.2×10^{-5} 9×10^{-6}
$H_{e,rms}$	0.177181 0.024747	0.176432 0.035412	0.182065 0.042913	0.177401 0.049293
$\sigma_{e,rms,MFop}^2$	0.354106 0.058617	0.392583 0.11411	0.440107 0.168050	0.522280 0.223486
C_BER	$< 1.95 \times 10^{-7}$	$\approx 9.76 \times 10^{-7}$	$\approx 1.17 \times 10^{-6}$	$\approx 3.9 \times 10^{-7}$

The RMS estimation error in various parameters is given in Table 2, at an average SNR per bit of 5 dB. The numbers in red colour correspond to ideal channel, that is

$$h(nT_s) = \delta_K(nT_s). \quad (50)$$

The numbers in blue are for fading channel as in (12). We can make the following observations from Table 2:

1. The RMS estimation errors for the fading channel is much higher than the ideal channel. This can be attributed to the ISI introduced by the fading channel.
2. The C_BER of the ideal channel is also much lower than that of the fading channels (Figures 7-10), at an SNR per bit of 5 dB. In fact, for $N_{sc} = 1$, there were zero errors out of 512×10^4 bits (less than one error out of 512×10^4 bits). Similarly, for $N_{sc} = 2, 3, 4$ there were less than 10 errors out of 512×10^4 bits, hence the C_BER is given as an approximation. This again indicates that the C_BER for fading channels is limited by ISI.

It was also observed from computer simulations that the RMS estimation errors for fading channels, as given in Table 2, is quite insensitive to wide variations in the SNR (0 – 25 dB), which can be attributed to ISI.

5. Conclusions

A new approach to OFDM-OQAM using the concept of single sideband modulation (SSB) has been discussed. The pulse corresponding to the square-root of the raised cosine (SRRC) spectrum and its modified Hilbert transform has been used to obtain bandwidth reduction by a factor of two. A simple matched filter is used at the receiver. The bit-error-rate (BER) performance of the proposed OFDM-OQAM system has been studied under various impairments such as carrier frequency offset (CFO), frequency selective Rayleigh fading channel and additive white Gaussian noise (AWGN). Discrete-time algorithms for frame detection, two-step CFO estimation, channel and noise variance estimation have been proposed. A single transmit and receive antenna is assumed. Similar work has not been done earlier. Future work could involve MIMO systems.

Conflicts of Interest: The author declares no conflicts of interest.

References

1. Vasudevan, K. Coherent detection of turbo coded OFDM signals transmitted through frequency selective Rayleigh fading channels. In Proceedings of the Signal Processing, Computing and Control (ISPC), 2013 IEEE International Conference on, Sept. 2013, pp. 1–6. <https://doi.org/10.1109/ISPC.2013.6663392>.
2. Vasudevan, K. Coherent Detection of Turbo-Coded OFDM Signals Transmitted Through Frequency Selective Rayleigh Fading Channels with Receiver Diversity and Increased Throughput. *Wireless Personal Communications* **2015**, *82*, 1623–1642. <https://doi.org/10.1007/s11277-015-2303-8>.
3. Vasudevan, K. Near Capacity Signaling over Fading Channels using Coherent Turbo Coded OFDM and Massive MIMO. *International Journal On Advances in Telecommunications* **2017**, *10*, 22–37. [Online].
4. Vasudevan, K. *Digital Communications and Signal Processing, Second edition (CDROM included)*; Universities Press (India), Hyderabad, www.universitiespress.com, 2010.
5. Farhang-Boroujeny, B. OFDM Versus Filter Bank Multicarrier. *IEEE Signal Processing Magazine* **2011**, *28*, 92–112. <https://doi.org/10.1109/MSP.2011.940267>.
6. Jiang, T.; Ni, C.; Qu, D.; Wang, C. Energy-efficient NC-OFDM/OQAM-based cognitive radio networks. *IEEE Communications Magazine* **2014**, *52*, 54–60. <https://doi.org/10.1109/MCOM.2014.6852083>.
7. Basar, E. Index modulation techniques for 5G wireless networks. *IEEE Communications Magazine* **2016**, *54*, 168–175. <https://doi.org/10.1109/MCOM.2016.7509396>.
8. Weitkemper, P.; Koppenborg, J.; Bazzi, J.; Rheinschmitt, R.; Kusume, K.; Samardzija, D.; Fuchs, R.; Benjebbour, A. Hardware experiments on multi-carrier waveforms for 5G. In Proceedings of the 2016 IEEE Wireless Communications and Networking Conference, April 2016, pp. 1–6. <https://doi.org/10.1109/WCNC.2016.7564682>.
9. Jin, C.; Hu, S.; Huang, Y.; Li, F.; Zhang, J.; Ma, S. On design of conjugated transmission scheme for FBMC/OQAM systems with interference cancellation. *China Communications* **2017**, *14*, 166–175. <https://doi.org/10.1109/CC.2017.8014377>.
10. Yang, F.; Wang, Y.; Ding, L.; Qian, L. An improved equalization with real interference prediction scheme of the FBMC/OQAM system. *China Communications* **2021**, *18*, 120–129. <https://doi.org/10.23919/JCC.2021.01.011>.
11. Alaghbari, K.A.; Lim, H.S.; Eltaif, T.; Jin, B.; Lee, L.H. Filterbank-Assisted Channel Estimation for Coherent Optical FBMC/OQAM System. *IEEE Photonics Journal* **2022**, *14*, 1–7. <https://doi.org/10.1109/JPHOT.2022.3228876>.

12. Lu, X.; Jiang, Y.; Wei, Y.; Tu, X.; Qu, F. A Lattice-Reduction-Aided Sphere Decoder for Underwater Acoustic FBMC/OQAM Communications. *IEEE Wireless Communications Letters* **2023**, *12*, 466–470. <https://doi.org/10.1109/LWC.2022.3230857>.
13. Qi, Y.; Dang, J.; Zhang, Z.; Wu, L.; Wu, Y. Efficient Channel Equalization and Performance Analysis for Uplink FBMC/OQAM-Based Massive MIMO Systems. *IEEE Transactions on Vehicular Technology* **2023**, *72*, 11532–11547. <https://doi.org/10.1109/TVT.2023.3263220>.
14. Hamdar, F.; Nadal, J.; Nour, C.A.; Baghdadi, A. Overlap-Save FBMC Receivers for Massive MIMO Systems. *IEEE Transactions on Wireless Communications* **2024**, *23*, 9643–9656. <https://doi.org/10.1109/TWC.2024.3364542>.
15. Rebouh, D.; Djebbar, A.B.; Besseghier, M. Blind Joint CFO and STO Estimation for FBMC/OQAM Systems. *IEEE Communications Letters* **2023**, *27*, 2422–2426. <https://doi.org/10.1109/LCOMM.2023.3293392>.
16. Qi, Y.; Dang, J.; Zhang, Z.; Wu, L.; Wu, Y. Downlink Precoding for Cell-Free FBMC/OQAM Systems With Asynchronous Reception. *IEEE Communications Letters* **2023**, *27*, 2427–2431. <https://doi.org/10.1109/LCOMM.2023.3294221>.
17. Hamdar, F.; Gussen, C.M.G.; Nadal, J.; Nour, C.A.; Baghdadi, A. FBMC/OQAM Transceiver for Future Wireless Communication Systems: Inherent Potentials, Recent Advances, Research Challenges. *IEEE Open Journal of Vehicular Technology* **2023**, *4*, 652–666. <https://doi.org/10.1109/OJVT.2023.3303034>.
18. Chen, D.; Luo, K.; Peng, W.; Wang, W. Low-Complexity Symbol Reconstruction Based on Direct Symbol Decision for FBMC-OQAM Systems. *IEEE Transactions on Signal Processing* **2023**, *71*, 4369–4381. <https://doi.org/10.1109/TSP.2023.3328061>.
19. Zhang, J.; Tan, H.; Lu, L.; Wu, X.; Hong, X.; Fei, C.; Lau, A.P.T.; Lu, C. Comparison of FBMC and OFDM With Adaptive Bit and Power Loading for CD-Constrained IM/DD Transmission Over 50-km SSMF. *Journal of Lightwave Technology* **2024**, *42*, 2702–2710. <https://doi.org/10.1109/JLT.2023.3342099>.
20. Punt, M.; Vui, D. Software Implementation and Cyclic Feature Characterization of Nu-FBMC/OQAM Signals. *IEEE Access* **2024**, *12*, 26636–26641. <https://doi.org/10.1109/ACCESS.2024.3367238>.
21. ubrilovi, S.; Kuzmanovi, Z.; Punt, M.; Vui, D.; Kovaevi, B. FBMC/OQAM-Based Secure Voice Communications Over Voice Channels. *IEEE Access* **2024**, *12*, 94452–94460. <https://doi.org/10.1109/ACCESS.2024.3424315>.
22. Chen, D.; Wei, H.; Chen, Y. Joint Prototype Filter and Symbol Distribution Optimization for Sidelobe Suppression of FBMC-OQAM Signals. *IEEE Transactions on Wireless Communications* **2025**, *24*, 4996–5008. <https://doi.org/10.1109/TWC.2025.3545427>.
23. Dai, L.; Wang, J.; Li, Y.; Chen, L.; Liang, X. FBMC-Chirp Waveforms for Joint Wireless Communication and SAR Imaging. *IEEE Transactions on Vehicular Technology* **2025**, *74*, 16065–16078. <https://doi.org/10.1109/TVT.2025.3571915>.
24. Li, L.; Zhang, J.; Ding, L.; Wang, Y.; Zhang, H. Low PAPR FBMC-OQAM System Based on Data Mapping and DFT Spreading. *IEEE Internet of Things Journal* **2025**, *12*, 22311–22324. <https://doi.org/10.1109/JIOT.2025.3550843>.
25. Chen, D.; Song, L.; Liu, P.; Luo, K.; Peng, W.; Wang, W. Phase Noise Estimation and Pilot Design Suppressing Intrinsic Interference for mmWave FBMC-OQAM Systems. *IEEE Transactions on Communications* **2025**, *73*, 12087–12099. <https://doi.org/10.1109/TCOMM.2025.3591155>.
26. Hamdar, F.; Nadal, J.; Nour, C.A.; Baghdadi, A. Efficient Filter-Bank Pilot Structures for Multi-User Massive MIMO Systems. *IEEE Transactions on Communications* **2025**, *73*, 14960–14973. <https://doi.org/10.1109/TCOMM.2025.3597802>.
27. Lin, T.T.; Chen, T.C. Efficient Channel Estimation for Universal Filtered Multicarrier Systems. *IEEE Systems Journal* **2021**, *15*, 3793–3796. <https://doi.org/10.1109/JSYST.2020.3019289>.
28. Choi, K. FD-FBMC: A Solution for Multicarrier Full Duplex Cellular Systems. *IEEE Communications Letters* **2021**, *25*, 617–621. <https://doi.org/10.1109/LCOMM.2020.3028375>.
29. Si, F.; Zheng, J.; Chen, C. Reliability-Based Signal Detection for Universal Filtered Multicarrier. *IEEE Wireless Communications Letters* **2021**, *10*, 785–789. <https://doi.org/10.1109/LWC.2020.3043735>.
30. Chen, C.; Zheng, J.; Si, F. Sparse Code Multiple Access Over Universal Filtered Multicarrier. *IEEE Transactions on Vehicular Technology* **2021**, *70*, 10335–10346. <https://doi.org/10.1109/TVT.2021.3106001>.
31. Zhang, C.; Gao, M.; Shi, Y.; Liu, X.; Chen, B.; Liu, G.N. Experimental Comparison of Orthogonal Frequency Division Multiplexing and Universal Filter Multi-Carrier Transmission. *Journal of Lightwave Technology* **2021**, *39*, 7052–7060. <https://doi.org/10.1109/JLT.2021.3113388>.
32. Jiang, R.; Fei, Z.; Cao, S.; Xue, C.; Zeng, M.; Tang, Q.; Ren, S. Deep Learning-Aided Signal Detection for Two-Stage Index Modulated Universal Filtered Multi-Carrier Systems. *IEEE Transactions on Cognitive Communications and Networking* **2022**, *8*, 136–154. <https://doi.org/10.1109/TCCN.2021.3101222>.
33. Kebede, T.; Wondie, Y.; Steinbrunn, J.; Kassa, H.B.; Kornegay, K.T. Multi-Carrier Waveforms and Multiple Access Strategies in Wireless Networks: Performance, Applications, and Challenges. *IEEE Access* **2022**, *10*, 21120–21140. <https://doi.org/10.1109/ACCESS.2022.3151360>.
34. Lin, T.T.; Hwang, F.H. Blind CFO Estimation in a UFMC System Aided With Virtual Carriers. *IEEE Transactions on Vehicular Technology* **2022**, *71*, 4495–4499. <https://doi.org/10.1109/TVT.2022.3146765>.

35. Lin, T.T.; Hwang, F.H. Design of a Blind Estimation Technique of Carrier Frequency Offset for a Universal-Filtered Multi-Carrier System Over Rayleigh Fading. *IEEE Wireless Communications Letters* **2022**, *11*, 1027–1031. <https://doi.org/10.1109/LWC.2022.3153309>.
36. Guner, M.T.; Sahab, A.S.; Seker, C. Performance analysis of modulation techniques in 5G communication system. *China Communications* **2022**, *19*, 100–114. <https://doi.org/10.23919/JCC.2022.08.008>.
37. Asgharnia, M.; Hosseini, S.A.; Shahzadi, A.; Ghazi-Maghrebi, S.; Kandovan, R.S. Optimization Framework for User Clustering, Beamforming Design and Power Allocation in MIMO-UFMC Systems. *IEEE Access* **2024**, *12*, 148916–148934. <https://doi.org/10.1109/ACCESS.2024.3422815>.
38. Tu, Y.P.; Hsu, C.W. A Low Complexity Dual-Phase Alternating Scheme is Used With the PTS Method to Reduce PAPR for B5G Systems. *IEEE Access* **2025**, *13*, 23971–23986. <https://doi.org/10.1109/ACCESS.2025.3538778>.
39. Dávila, M.; Arguero, B.; Tipantuña, C.; Arévalo, G.V.; Camacho, J.; Parra, C.; Hesselbach, X. Implementation of a Radio-Over-Fiber System Based on UFCM for the Coming 6G Mobile Networks. *IEEE Access* **2025**, *13*, 177258–177268. <https://doi.org/10.1109/ACCESS.2025.3616962>.
40. Eren, T. Low-Complexity Universal Filtered Multi-Carrier Receiver and Pilot-Aided Channel Estimation for 6G OFDM Waveforms. *IEEE Access* **2025**, *13*, 174720–174731. <https://doi.org/10.1109/ACCESS.2025.3618780>.
41. Vasudevan, K.; Kota, S.; Kumar, L.; Mishra, H.B. Turbo Coded OFDM-OQAM using Hilbert Transform. In Proceedings of the Sustainable Industrial Processing Summit and Exhibition, 2023, Vol. 15, pp. 213–228.
42. Vasudevan, K.; Kota, S.; Kumar, L.; Mishra, H.B. Scilab Code for Turbo Coded OFDM-OQAM using Hilbert Transform. <https://www.codeocean.com/>, 2024. <https://doi.org/10.24433/CO.1589250.v1>.
43. Haykin, S. *Communication Systems*, second ed.; Wiley Eastern, 1983.
44. Vasudevan, K. Coherent Turbo Coded MIMO OFDM. In Proceedings of the ICWMC 2016, The 12th International Conference on Wireless and Mobile Communications, Nov. 2016, pp. 91–99. [Online].
45. Vasudevan, K.; Madhu, K.; Singh, S. Data Detection in Single User Massive MIMO Using Re-Transmissions. *The Open Signal Processing Journal* **2019**, *6*, 15–26. <https://doi.org/10.2174/1876825301906010015>.
46. Vasudevan, K.; Singh, S.; Reddy, A.P.K. Coherent Receiver for Turbo Coded Single-User Massive MIMO-OFDM with Retransmissions. In *Multiplexing*; Mohammady, S., Ed.; IntechOpen: London, 2019; chapter 4, pp. 1–21. <https://doi.org/10.5772/intechopen.85893>.
47. Vasudevan, K.; Pathak, G.K.; Reddy, A.P.K. Turbo Coded Single User Massive MIMO with Precoding. In Proceedings of the Proc. of the 1st IFSA Winter Conference on Automation, Robotics & Communications for Industry 4.0 (ARCI 2021), Chamonix-Mont-Blanc, Feb. 2021; pp. 6–11.
48. Vasudevan, K.; Phani Kumar Reddy, A.; Gyanesh Kumar Pathak.; Mahmoud Albreem. Turbo Coded Single User Massive MIMO. *Sensors & Transducers Journal* **2021**, *252*, 65–75.
49. Vasudevan, K.; Kota, S.; Kumar, L.; Mishra, H.B. New Results on Single User Massive MIMO. In *MIMO Communications - Fundamental Theory, Propagation Channels, and Antenna Systems*; Kishk, D.A.; Chen, D.X., Eds.; IntechOpen: Rijeka, 2023; chapter 17. <https://doi.org/10.5772/intechopen.112469>.
50. Proakis, J.G.; Manolakis, D.G. *Digital Signal Processing: Principles, Algorithms and Applications*, second ed.; Maxwell MacMillan, 1992.
51. Vasudevan, K. *Analog Communications: Problems & Solutions*; Ane Books, Springer, 2018.
52. Vasudevan, K.; Phani Kumar Reddy, A.; Pathak, G.K.; Singh, S. On the Probability of Erasure for MIMO OFDM. *Semiconductor Science and Information Devices* **2020**, *2*, 1–5. <https://doi.org/10.30564/ssid.v2i1.1689>.
53. Bahl, L.; Cocke, J.; Jelinek, F.; Raviv, J. Optimal Decoding of Linear Codes for Minimizing Symbol Error Rate. *IEEE Trans. on Info. Theory* **1974**, *20*, 284–287.

Disclaimer/Publisher’s Note: The statements, opinions and data contained in all publications are solely those of the individual author(s) and contributor(s) and not of MDPI and/or the editor(s). MDPI and/or the editor(s) disclaim responsibility for any injury to people or property resulting from any ideas, methods, instructions or products referred to in the content.